Preparation and characterization of copper based cermet anodes for use in solid oxide fuel cells at intermediate temperatures

N. E. Kiratzis · P. Connor · J. T. S. Irvine

Abstract Two Cu-based anode cermets suitable for direct hydrocarbon oxidation in Solid Oxide Fuel Cells (SOFC) based on yttria stabilized zirconia (YSZ) electrolyte were tested in the temperature range (500–800°C). The ceramic components were CeO_2 and the perovskite $La_{0.75}Sr_{0.25}Cr_{0.5}Mn_{0.5}O_{3-d}$ (LSCM). The cermets were made in both the form of pellets and films applied onto the YSZ electrolytes. Pellets exhibited good mechanical strength and resistance to fracture in both oxidized and reduced state. Cu–LSCM cermets exhibited good redox cycling behavior between 700–800°C. Reduction temperature plays a significant role on final morphology with Cu segregation occurring at 800°C. Cu–LSCM films were found to exhibit lower polarization resistances than Cu–CeO_2 under 5% H_2. Examination of the data revealed a poorer contact of the Cu–CeO_2 electrode with the YSZ surface than the Cu–LSCM electrode. Reduction temperature should be less than 750°C to ensure suitable microstructure and adhesion of both film electrodes with the electrolyte.

Keywords SOFC · Cu anodes · Cermet · LSCM · CeO_2

P. Connor · J. T. S. Irvine
School of Chemistry, University of St. Andrews,
St Andrews,
Fife KY16 9ST Scotland, UK

N. E. Kiratzis (✉)
Technological Research Center (TRC),
Technological Education Institute (TEI) of West Macedonia,
Kozani 50100, Greece
e-mail: kiratzis@teikoz.gr

1 Introduction

Fuel cells are considered for replacement of conventional thermal electricity production systems, mainly because of their inherently high efficiency, as well as their low pollutant emissions. Solid oxide fuel cells (SOFC) operate by means of a ceramic electrolyte at temperatures typically above 500°C in order to achieve sufficient values of ionic conductivity. Ionic conduction is provided by oxygen ions in the most widely used solid electrolytes of mixed oxides of yttria/zirconia (YSZ) or ceria/gadolinia (CGO), but also by hydrogen ions in other types of ceramic materials such as $BaZr_{0.9}Y_{0.1}O_{2.95}$ [1]. These high temperature operating cells offer several other advantages: They produce high quality heat as a by-product for use in Combined Heat and Power (CHP) applications. They are also more fuel flexible with carbon monoxide being a fuel rather than a poison in this type of fuel cell. There also exists the potential for internal reforming of hydrocarbon fuels inside the fuel cell. A good review of the types of solid electrolytes and their applications in industrially important catalytic reactions is given by Stoukides [2].

Traditionally, Ni–YSZ cermets have been used as anodes due to their low cost and high activity for hydrogen oxidation. In addition, nickel is very active in promoting steam reforming of methane. The latter is exploited in the internal reforming operation of a SOFC in which a fuel mixture of methane and water is introduced into the cell and reacts over the nickel cermet anode. However, this type of anode under a reducing hydrocarbon atmosphere also catalyses the formation of carbon filaments above 700°C due to the activity of Ni for this undesirable reaction. Thus, generally, high steam-to-carbon ratios are required in order to suppress carbon formation in the above systems [3]. Another problem associated with the use of these Ni-based

anodes for operation at temperatures above 700°C is the sintering and growth of Ni particles in poorly prepared or non-optimized Ni–YSZ cermets [4].

The present study is concerned with the development of a suitable anode for solid oxide fuel cells operated on natural gas or other hydrocarbons in the absence of significant amounts of steam. S. McIntosh and R. J. Gorte give a good review on the properties of this type of anodes and adopted approaches [5]. The general requirements for such an anode include adequate electronic conductivity and simultaneously high electrocatalytic activity with low overpotential loss. However, this catalytic activity should not extend to undesirable side reactions such as carbon formation in the case of hydrocarbon fuels. In addition, it should exhibit good adhesion to electrolyte and allow for fast mass transfer rates of the fuel and the reaction products to and from the gas phase. The latter requires an optimized microstructure, which is dependent on the adopted fabrication method. Other desirable characteristics include chemical stability and compatibility, thermal expansion compatibility, and mechanical strength and dimensional stability under redox cycling. It has been established that the charge transfer reaction is located on the "three phase boundary" zone encompassing the electrolyte–electrode–gas phase contact area.

It would be advantageous to replace Ni-cermets with mixed conducting (i.e. ionic and electronic) electrodes, as this would significantly increase the available electrode surface area for electrochemical reaction leading to lower anodic overpotentials and thus, superior cell performance [6]. In addition, lattice oxygen participates in the oxidation of hydrocarbons [7, 8]. Mixed conductivity is exhibited by $Ce_{0.9}Gd_{0.1}O_{1.95}$ (CGO10) under the fuel reducing conditions and above 600°C due to the conversion of Ce^{4+} ions to Ce^{3+} ions. This material has been tested as anodic electrode for methane oxidation at 900°C and has been found to exhibit low levels of carbon formation, accompanied, however, by a relatively low activity towards methane oxidation [9, 10]. In contrast to CGO10, undoped ceria is a well-known effective oxidation catalyst, which is attributed to the differing electronic functionalities of the doped and undoped materials [4]. Very encouraging results were obtained on composite anodes of the type $Cu/CeO_2/YSZ$ under SOFC operating conditions with a variety of hydrocarbon fuels [11–16]. Cu and CeO_2 in these anodes were added by wet impregnation of nitrate salts to a porous YSZ anode matrix. Copper appears to act as an electronic conductor while being inert to hydrocarbon oxidation. Thus, the combination of copper and a good oxidation catalyst, such as CeO_2, seems to be a good strategy for designing suitable anodes for the direct (i.e. without the need of reforming) oxidation of hydrocarbons in SOFCs. Cu, however, exhibits poor thermal stability, especially

above 900°C, due to sintering [17, 18]. In fact, it has been found that annealing under H_2 at temperatures above 700°C results in significant drops in both bulk conductivity and fuel cell performance of $Cu/CeO_2/YSZ$ cermets prepared as described above. At 900°C Cu segregation is severe, forming either isolated particles or even extended porous films near the YSZ surface depending on the type of impregnation salts used for the anode fabrication [18, 19]. In addition, CeO_2–YSZ interfaces constitute a quite interesting system; these interfaces have been shown to be dynamic in nature, with CeO_2 being quite mobile and redistributed over the YSZ surface upon exposure to reducing conditions [20].

Other oxides of interest as potential anodes include transition metal perovskites and fluorite-related structures. Doped fluorite oxides with Ti or Nb allows for the introduction of electronic conductivity into the material due to the reduction of the transition metal under the fuel conditions prevailing at the anode side of the fuel cell. This concept has been tested in a composite anode of the type $Cu/Y_{0.2}Ti_{0.18}Zr_{0.62}O_{1.9}$ (Copper/Yttria Titania Zirconia or Cu/YZT) [21]. It was found that this cermet could be successfully redox cycled, exhibiting high conductivity values under a wide range of oxygen partial pressures. Co-sintering of Cu and YZT resulted only in a small amount of reaction between the components causing a slight tetragonal distortion of YZT. Electrochemical performance measured in a three-electrode geometry was good for hydrogen oxidation up to about 800°C. Copper agglomeration, however, was observed at higher temperatures.

Oxidation of hydrocarbons can take place on a number of materials based on lanthanum chromate, that offer improved resistance to cracking reactions at low steam partial pressures. The performance of such oxide electrodes with perovskite, fluorite and related structures is discussed by Irvine and Sauvet [22]. More specifically, a typical perovskite used as interconnect material is $La_{1-x}Sr_xCrO_3$ [23]. This material exhibits quite good stability [24] in both reducing and oxidizing conditions at high temperatures and for this reason it can also be used as anode. Substitution of mid-transition metals (e.g. Mn or Fe) on the B-site has been shown to improve catalytic activity towards methane reforming [25]. This strategy has been tested on a lanthanum chromium manganite of the formula $(La_{0.75}Sr_{0.25})Cr_{0.5}Mn_{0.5}O_{3d}$(LSCM) [26–31] which combines the good catalytic properties of lanthanum manganite with the stability and conductivity of chromite, without diluting Cr on the B-site. This material exhibits predominant p-type conductivity in oxidizing and moderately reducing atmospheres. Under reducing conditions it exhibits ionic conductivity, though the total conductivity becomes lower. It was found that this material exhibits good chemical compatibility with YSZ up to 1300°C. Very

good electrochemical performance was achieved in terms of polarization resistance in wet H_2 either by mixing the material with a small amount of YSZ or inserting a thin layer of $Ce_{0.8}Gd_{0.2}O_{2-\delta}$ (CGO20) between the YSZ and the LSCM anode [27]. The material also demonstrated very good performance under methane above 700°C, as well as good redox stability without using excess steam, promoting full rather than partial oxidation [32]. These favorable properties have been tested successfully in the performance of symmetrical cells (i.e. cells with the same material used as both cathode and anode) using either LSCM or a composite of the type LSCM–(YSZ–CGO) [33, 34]. However measured conductivities of this material did not exceed 10 S cm^{-1} under reducing conditions. Recently, however, it has been shown that its electrochemical performance can be significantly improved by mixing it with a Cu–YSZ cermet [35].

Comparison of performance between LSCM, Cu–CeO$_2$ and Ni–YSZ anodes as reported in the literature is shown in Table 1. Values are given for polarization resistances, maximum power outputs, and overpotentials in the presence of H_2 or other carbon containing gases such as natural gas (NG), CO or synthesis gas (SG). In addition, values for long term performance and sulfur tolerance in terms of ppm H_2S are provided.

Ni/YSZ has been recognized as the universal anode material for SOFCs and has been extensively studied and optimized after the pioneering work of Westinghouse in the 1970s. Its superior performance in H_2 is shown in terms of polarization resistance in Table 1 with values as low as 0.03–0.16 Ω cm^2 in the temperature range 850–1000°C [6, 36]. Higher values are also reported [37] and this variation is due to the differences in the cermet microstructure, which in turn depends on the adopted fabrication method and thermal treatment histories before and after the application of the anodic electrode. Operating conditions also affect the microstructure and degradation rates. Low polarization resistances were also reported at lower temperatures (i.e. 600°C) by Murray et al. [38] on a Ni–YSZ modified electrode that was formed as composite with Yttria doped Ceria (YDC). Anodic polarization resistance values for Cu–CeO$_2$ and LSCM electrodes under H_2 are reported between 0.1 and 0.8 Ω cm^2 (see Table 1) and compare favorably with those of Ni–YSZ. It has to be stressed, however, that these latter anodes were developed essentially for use with hydrocarbons than H_2 in order to replace Ni, which promotes carbon formation at temperatures above 750°C. Cu–CeO$_2$ and modified Cu–CeO$_2$ anodes were developed by Gorte and collaborators who adopted a specific fabrication method as described previously [39–43]. These anodes exhibited superior values of anodic polarization resistances under CH$_4$, C$_4$H$_{10}$, CO and synthesis gas in the temperature range 700–800°C. LSCM anodes also showed encouraging polarization resistances under CH$_4$ at higher temperatures (i.e. 800–900°C [27, 44, 45]. In contrast, Ni–YSZ cermets could only be used with CH$_4$ at lower temperatures and exhibited quite high polarization resistance (i.e. 6.5 Ω cm^2) at 600°C. This value was improved only by application of a composite YDC/Ni–YSZ anode [38].

Ni–YSZ anodes exhibit superior performances in terms of maximum power densities under H_2 proving that Ni is an excellent electrocatalyst for H_2 oxidation. It has to be emphasized here, that maximum power densities depend on the thickness of the dense electrolyte layer and hence on the cell fabrication method adopted. Higher power densities are realized in planar configuration anode or cathode supported cells employing thin electrolytes [46, 47]. Maximum power densities for Ni–YSZ cermets were in the range of 1.3–1.7 W/cm^2. The highest value was obtained using a Ni–YSZ supported cell consisting of a 10 μm YSZ–Samaria doped Ceria(SDC) bilayer and a La$_{1-x}$Sr$_x$CoO$_{3-\delta}$ (LSC)–SDC cathode [48]. Cathode supported planar cells have also shown encouraging performance at lower temperatures (i.e. 650°C) in wet H_2 by employing composite anodes of Ni–YSZ/YDC with YDC/LSM composite cathodes [49].

In the presence of CH$_4$, Ni–YSZ cermets tend to promote carbon formation especially under open circuit conditions but under current, values of 0.96 A/cm^2 are reported at 800°C in a planar 25 μm YSZ electrolyte anode supported cells [50]. Good performance is also obtained under synthesis gas, probably because of the presence of H_2 [47]. Lower power density values were obtained on Cu–CeO$_2$ anodes but these were usually taken on a 60 μm YSZ electrolyte [11]. Higher values were obtained under H_2 by alloying the Cu with either Ni or Co, which also provide better thermal stability [51, 41]. Interestingly, low levels of Ni promote the formation of moderate levels of carbon that improved performance. In the presence of other than H_2 compounds, modified (in terms of alloying Cu with Co) Cu–CeO$_2$ anodes exhibit maximum current densities of the order of 0.36–0.37 A/cm^2 with CO, synthesis gas or n-butane at temperatures 700–800°C [41, 43]. These values are actually higher than those under H_2 and are also comparable with those obtained on isooctane or CH$_4$ fuel on a Ni–YSZ anode with a 8–10 μm YSZ electrolyte [52, 38] and even to H_2 operating Ni–YSZ cells [48] after taking into account the differences in electrolyte thickness. Maximum values for CH$_4$ fuels are in the range of 0.27–0.33 W/cm^2 for Cu–CeO$_2$ anodes which are comparable with Ni–YSZ performance after taking into account the electrolyte thickness and the added advantage of the absence of carbon formation [51, 14]. In fact, higher molecular weight hydrocarbons such as n-decane and diesel were also used successfully with obtained power densities of the order of 0.1 W/cm^2 at 700°C [12].

Table 1 Performance characteristics of Cu–CeO2, LSCM and Ni–YSZ anodes.

	LSCM	LSCM[a] modified	Cu–CeO2	Cu–CeO2 modified	Ni–YSZ	Ni–YSZ modified	References
Rp, Ω cm² in H_2	0.37–0.7 (925°C)	0.25–0.62 (850–950°C)	0.4–0.8 (710°C)	<0.1[b] (700°C)	0.03–0.16[c] (850–1000°C) 0.14–2.7 (850–1000°C) 0.23–7 (700–850°C)	0.25–1.1[d] (600°C)	[6], [27], [36], [37], [39–41]
Rp/Ω cm² in others		0.44 (800°C)[e] 0.87 (900°C)[e]	0.4–0.6[f,g] (700°C)[h] 0.9[i] (800°C)[h]	0.35[j] (700°C)[k]	6.5 (600°C)[e]	1.1[d] (600°C)[e]	[27], [38], [39], [42–45]
Max. power density/W/cm² in H_2	0.5 (950°C)	0.29–0.47[l] (900°C)	0.22–0.30[f] (700°C) 0.31–0.42 (800°C)	0.33–0.34[m] (700°C) 0.44–0.57[o] (800°C)	0.57–0.8[p] (750°C) 0.85–1.3[p] (800°C)	0.48[d] (650°C) 0.87[d]–1.7[q] (800°C)	[11], [27], [37], [40], [41], [43], [46–49], [51], [53]
Max. power density/W/cm² in others	0.3 (950°C)[e]	0.2 (900°C)[e]	0.25–0.30[f] (700°C)[k] 0.1–0.12[r] (700°C) 0.30 (800°C)[s] 0.11–0.27 (800°C)[h]	0.36–0.37[j] (700°C)[k] 0.12–0.15[t] (700°C) 0.36[o] (800°C)[s] 0.25[o]–0.33[n] (800°C)[h]	0.34[u] (750°C) 0.8 (800°C)[v] 0.96[w] (800°C)[e,x]	0.37[d] (650°C)[e]	[11], [12], [14], [27], [41–43], [47], [50–53]
Overpotential, V			0.08–0.4[f] (700°C)[y] 0.1–0.2[f] (700°C)[z] 0.53 (700°C)[aa]		≈0.3[f] (700°C)[y] 0.234 (800°C)[bb] 0.03–0.04 (1000°C)[cc]	0.056–0.15[dd] (800°C)[bb]	[37], [43], [54–56]
Long term performance	120 h (900°C)[ee]	7 h (900°C)[e]	48 h (700°C)[ff] 3 d (800°C)[h] 12 h (700°C)[gg]	48 h[hh] (900°C)[ii] 500 h[o] (800°C)[e]	80,000 h[jj] (>850°C)[ii] 8,000 h[kk] (1000°C)[ii] 2,500[ll]–4,800[mm] h (1000°C)[mm] 5,000 h[oo] (>850°C)[x] 1,000 h[pp] (950°C)[qq] >40–90 h[w] (700°C)[rr]	100 h[d] (550–650°C)[e]	[6], [11], [12], [19], [23], [26], [27], [37], [42], [47], [50], [57], [58]
Sulfur tolerance, ppmH_2S			450 (800°C)		0.05 (800°C) 2 (1000°C)		[16], [59]

[a] Either with Gadolinia doped ceria (GDC) as a composite of GDC/LSCM or graded LSCM-YSZ in contact with the YSZ electrolyte

[b] With $Cu_{0.7}Ni_{0.3}$ after exposure to n-butane for 2 h at 700°C, $j=0.3$ A/cm²

[c] Anodes produced at Risø National Laboratory, Denmark by spray painting

[d] Ni–YSZ/YDC composite anode and YDC/LSM composite cathode in cathode supported cells

[e] In wet CH4

[f] Cathode supported cells with LSF–YSZ cathode and 60 μm YSZ electrolyte

[g] In n-butane, CO or SG ($j=0.15$–0.4 A/cm²)

[h] In dry CH4

[i] $j=0.3$ A/cm^2

[j] Anode (Cu–Co(1:1)–CeO2–YSZ) supported cells with LSF–YSZ cathode and 60 μm YSZ electrolyte; Rp taken at $j=0.15$ A/cm^2

[k] In CO, SG

[l] Graded LSCM anode with 300 μm YSZ electrolyte

[m] Either on Cu$_{0.7}$Ni$_{0.3}$ or Cu$_{0.5}$Co$_{0.5}$ after exposure to n-butane for 2 h at 700°C

[n] Cu–20% Ni alloy after 500 h of operation; carbon formed at moderate levels improved performance

[o] On Cu$_{0.5}$Co$_{0.5}$–CeO$_2$–YSZ anode

[p] Higher values are reported for planar anode supported cells

[q] Anode consisted of an 10 μm YSZ–SDC bilayer on a Ni–YSZ supported cell with a La$_{1-x}$Sr$_x$CoO$_{3-\delta}$ (LSC)–SDC cathode; pure H$_2$

[r] In n-decane, toluene, diesel (diluted in N$_2$) or C$_4$H$_{10}$ with 60 μm YSZ electrolyte and after exposure to n-butane for 2 h at 700°C (for C$_4$H$_{10}$)

[s] In C$_4$H$_{10}$

[t] In C$_2$H$_6$, C$_4$H$_8$, C$_4$H$_{10}$ with 60 μm YSZ electrolyte and anodes of Cu–SDC (for C$_4$H$_8$, C$_4$H$_{10}$) and either Cu$_{0.7}$Ni$_{0.3}$ or Cu$_{0.5}$Co$_{0.5}$ after exposure to n-butane for 2 h at 700°C (for C$_4$H$_{10}$)

[u] 5.3% isooctane in N$_2$ in a 10 μm YSZ electrolyte anode supported cell

[v] In SG

[w] In a planar 25 μm YSZ electrolyte anode supported cell (severe carbon deposition observed at OCV)

[x] In NG

[y] 0.3 A/cm^2, H$_2$

[z] 0.3 A/cm^2, CO

[aa] 0.3 A/cm^2 C$_4$H$_{10}$

[bb] 0.25 A/cm^2, H$_2$

[cc] 0.2 A/cm^2, H$_2$

[dd] Ion impregnation with Sm$_{0.2}$Ce$_{0.8}$(NO$_3$)$_x$

[ee] 5% wet H$_2$

[ff] 0.12 A/cm^2, d.C$_4$H$_{10}$

[gg] n-decane, toluene, diesel

[hh] Co electrodeposited (5%) Cu–CeO$_2$ anode

[ii] wet H$_2$

[jj] Single tubular cells, Siemens-Westinghouse technology

[kk] Ni/YSZ powder made by spray pyrolysis

[ll] Coarse and fine YSZ co-sintered with NiO

[mm] Electrochemical vapor deposition (EVD) of YSZ on Ni under reducing conditions

[nn] 0.2–0.45 A/cm^2 w.H$_2$

[oo] 3 kW tubular stack (Siemens-Westinghouse technology) in desulfurized natural gas at 110 A

[pp] Flat planar electrolyte supported SOFC

[qq] 0.4 A/cm^2, d.CH$_4$

[rr] 0.6 V, w.CH$_4$ or NG

Power densities of the order of 0.5 W/cm^2 under H$_2$ were obtained on LSCM anode and a relatively thick YSZ electrolyte of 250–300 μm at 900–950°C using either graded LSCM compositions in contact with the YSZ [27] or in a symmetric fuel cell configuration (i.e. LSCM used as both anode and cathode) [53]. These power values are reduced to about a half under CH$_4$ but compare favorably with either Cu–CeO$_2$ or Ni–YSZ cermets though taken at higher temperatures but without again the formation of carbon deposits.

Overpotentials are also a measure of fuel cell performance and they have been measured in some studies under current load for Ni–YSZ and Cu–CeO$_2$ cermets. The corresponding polarization resistances can be estimated through mathematical derivatization with respect to current densities. It can be seen from Table 1 that measured values for the Cu–CeO$_2$ cermets are quite low of the order of 0.08 V [43] at low temperatures (i.e. 700°C) and match quite well values obtained for Ni–YSZ cermets at higher temperatures (i.e. 800–1000°C) [37, 54, 55]. In a comparative study of Cu–CeO$_2$ and Ni–YSZ anodes prepared similarly and thus, exhibiting similar porosities and microstructures [43], it was found that while Cu–CeO$_2$ anodes showed similar performance when operating under H$_2$ or CO, Ni–YSZ anodes exhibited significantly inferior performance under CO compared with H$_2$. Under H$_2$, both cermets exhibit similar overpotential values (see Table 1) but a different oxidation kinetics mechanism was identified for the two cermets: a positive order in P$_{H2}$ for the Cu–CeO$_2$ cermet and a nearly zero order for the Ni–YSZ cermets. However, H$_2$O had a minor effect on the H$_2$ oxidation kinetics on both cermets. As can be seen from Table 1, overpotentials measured under CO on Cu–CeO$_2$ anodes were even smaller than those under H$_2$ in the same temperature [43], and comparable to Ni–YSZ cells under H$_2$. Higher overpotentials (of the order of 0.5 V) were measured for n-butane [56].

In terms of long term performance values, Ni–YSZ undoubtedly is favored, as single tubular cells based on the Siemens-Westinghouse (SW) technology have been successfully tested for 80,000 h [47]. This technology, which has been studied and optimized since the 70s, produces a microstructure exhibiting very small degradation rates. It is based on a fabrication method involving electrochemical vapor deposition (EVD) of YSZ on a Ni skeletal structure under reducing conditions. This specific structure might be difficult to reproduce but co-sintering coarse and fine YSZ with NiO [6] resulted in reasonable values of long term performance (i.e. 2,500 h at 0.2 A/cm^2 and 1000°C). Good long term performance was also reported for cermets produced from composite powders from spray pyrolysis [37]. Ni–YSZ has also been tested in a 3 kW stack (SW technology) at 110 A under desulfurized natural gas for

5,000 h showing the beneficial effect of current on preventing carbon deposits [23]. This has also been shown by Weber et al. [57], who operated a planar electrolyte supported SOFC for 1,000 h under dry CH$_4$ at 0.4 A/cm^2 at 950°C. Operation under wet CH$_4$ or natural gas at 700°C (at 0.6 V) for 40–90 h has also been shown for anode supported flat cells by Liu and Barnett [50].

More data is definitely needed for long term testing of both Cu–CeO$_2$ and LSCM based anodes. Best performances of Cu–CeO$_2$ anodes are reported for CH$_4$ at 800°C. These were run for 3 days under dry CH$_4$ for an unmodified Cu–CeO$_2$ anode [58] and 500 h under wet CH$_4$ on Cu$_{0.5}$Co$_{0.5}$–CeO$_2$–YSZ anode [42] with Co improving significantly thermal stability and resistance of Cu–CeO$_2$ anodes to carbon formation. Thermal stability is also improved under H$_2$ even at 900°C (maximum 48 h) with Co electrodeposited (5%) Cu–CeO$_2$ anode [19].

Stability of Cu–CeO$_2$ anodes in other hydrocarbons (such as n-butane, n-decane, toluene and diesel) has also been demonstrated [11, 12]. These tests were conducted in a laboratory scale and definitely more tests are required for these anodes in larger scale stack configurations. This is also true for LSCM based anodes, which have been shown to exhibit phase stability for 120 h [26] and stability under wet CH$_4$ for 7 h [27]. Performance in wet H$_2$ was higher than in wet 5% H$_2$ with maximum power densities of 0.47 W cm^{-2} and 0.29 W cm^{-2} respectively at 900°C. More tests verifying long test stability under 100% H$_2$ are required.

Finally, in terms of sulfur tolerance Ni–YSZ anodes are very sensitive and suffer degradation for H$_2$S concentrations even above 2 ppm at 1000°C. This limit value is significantly lowered at lower temperatures as can be seen from Table 1 [59]. Cu–CeO$_2$ anodes, on the other hand, have been shown to withstand much higher concentrations up to 450 ppm at 800°C [16], which make them more suitable for direct hydrocarbon utilization.

Overall, Table 1 reveals that while Cu–CeO$_2$ and LSCM based anodes match adequately well the established Ni–YSZ anodes in terms of polarization resistances and power densities, more testing is needed in terms of their long term performance. These anodes offer the major advantage of direct hydrocarbon utilization of hydrocarbons in a SOFC without promoting carbon deposits. Their performance under CO or synthesis gas can be exceptional and in some cases exceeds performance under H$_2$. Their sulfur tolerance (for the Cu–CeO$_2$ anodes) also is significantly improved with respect to Ni–YSZ cermets.

In the present communication we seek to combine the properties of Cu as a catalytically inert but highly conductive metal with the favorable electrocatalytic properties of CeO$_2$ and La$_{0.75}$Sr$_{0.25}$Cr$_{0.5}$Mn$_{0.5}$O$_{3-\delta}$. For this purpose, we have fabricated slurries of cermets containing

copper and one the above oxides by conventional fabrication techniques. The same cermets were also formed as pellets by standard solid-state reaction techniques in order to check their suitability as anodic supports of thin electrolyte films. Thin electrolyte films supported on anodic electrodes are more suitable configurations for operation at low temperatures due to the significant reduction in the ohmic electrolyte resistance. These pellets were examined and characterized for phase purity, morphology, electrical conductivity and red-ox cycling stability.

For electrochemical testing we focus on the low to intermediate temperature regime (i.e. 500–700°C) in order to test the behavior of the above advanced anodes at lower temperatures. Lowering the temperature of a SOFC cell without compromising electrode kinetics is very desirable, especially for smaller units not coupled to a turbine as this would lead to higher efficiencies and relax material selection requirements allowing the use of more conventional materials for sealing and interconnection.

Moreover, Cu has a relatively low melting temperature (1083°C) and has been found to segregate even above 700°C [18]. Thus, the use of Cu based anodes limits the operation of a SOFC based on such types of anodes to the intermediate temperature range. Thus, it is necessary to explore ceramics combined with Cu, which are catalytically active in this low to intermediate temperature range.

In addition, the low operating temperatures offer the advantage of focusing more on the electrocatalytic effect on the charge-transfer mechanism, as this is more likely to dominate. The selected ceramic materials have been found [11–16, 32] to exhibit an improved electrochemical reaction zone for either H_2 or CH_4 oxidation, which renders them suitable in this temperature regime.

As a first step towards this goal, we employed AC impedance analysis of symmetrical YSZ cells under hydrogen at close to open circuit conditions to concentrate on purely electrocatalytic effects avoiding complications due to the effect of overpotential.

2 Materials and methods

Pellets of cermets of Cu/LSCM and Cu/CeO$_2$ were made from the original oxide powders by the solid-state reaction (SSR) technique. Specifically, for the Cu/CeO$_2$ cermet, powders of CuO (Sigma-Aldrich) and CeO$_2$ (Alfa Aesar) or LSCM were ground in a mortar and pestle under ethanol for about 45 min. The resulting powder was left to dry overnight and subsequently was pressed to pellets at ≈490 MPa. The pellets were then sintered in air at 1000°C for 10 h, heating at 5°C/min and cooling at 10°C/min. This procedure produced pellets of reasonable mechanical strength and minimal cracks. Average particle sizes for CeO$_2$ and CuO were 5 μm and 8 μm respectively as given by the manufacturers.

For the Cu/LSCM cermet, the original LSCM powder was prepared from the original oxides by the SSR technique and sintered at 1400 °C for 38 h in air. Powders made this way exhibit an average surface area of about 1 m^2/g [53] from which we can calculate an average particle size of about 0.9 μm. Characterization of this powder had been done by XRD [27]. Then, CuO and the prepared LSCM powder were processed exactly as described previously for the Cu/CeO$_2$ cermet to yield the final product.

Four-point DC conductivity measurements were performed on a Cu/LSCM pellet in a vertical conductivity jig using platinum paste electrode contacts linked via platinum foil to platinum leads. Measurements were performed using a zirconia sensor to monitor oxygen partial pressure. A reducing atmosphere was achieved by allowing either 5% H$_2$ in Ar or Ar into the vessel. The return to oxidizing conditions was allowed to occur slowly through a controlled leak into the furnace. Conductivity and oxygen partial pressure were monitored during this change. Measurements started on an already reduced pellet (1000°C for 2 h). Pellet conductivity was measured at 968 and 1070 K as function of oxygen partial pressure in the range 10^{-22}–0.2 atm. Conductivity was also measured under reducing conditions (5% H$_2$) as function of temperature during heating. The same was also done under oxidizing conditions (pO$_2$=0.20 atm) during a cooling cycle from 1067 to 967 K.

Actual pellet densities were measured by means of a He pycnometer (QUANTACHROME Corp., SYOSSET, NY 11701, USA).

Slurries of the above cermets were also prepared for electrochemical measurements. These were made by mixing the appropriate starting oxide powders with organic solvents. Specifically, for the Cu–CeO$_2$ slurry, CuO and CeO$_2$ powders were used with a mixture of methyl ethyl ketone (MEK)–ethanol (3:2 v/v) (Sigma-Aldrich) (typically 40–50% w/w of dry powder) as the carrier liquid, with Triton as dispersant (at 0.6–1.5% per weight of dry powder). The dispersion was initially shaken for about 20 min by a vibratory mill and then was ball milled for 18 h. This was followed by the addition of the Butvar binder (Sigma-Aldrich) (10% per weight of dry powder) and subsequent ball milling for about 5 h. The same procedure was followed for the preparation of the Cu–LSCM slurry except that isopropanol was used as carrier.

The above slurries were painted onto dense YSZ pellets. These had a thickness of about 300 μm (8% Yttria stabilized zirconia or 8 YSZ) and were provided by (CeramTec, Germany). All electrolyte pellets used for electrode painting were ground on SiC paper before painting. The painted pellets were sintered in air at
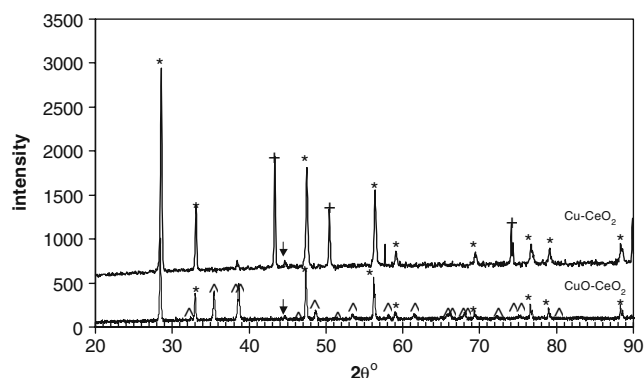
Table 2 Composition of fabricated cermets.

Sample #	Type	CuO, % w/w	Porosity/oxidized,%	Porosity/reduced, %
Pellets				
1	Cu–CeO$_2$	48.986	21.4	41.0
2	Cu–CeO$_2$	59.438	23±2	45.8
3	Cu–LSCM	49.206	33.2	47.8 (calc)
4	Cu–LSCM	61.981	37±1	53.5
Slurries			Carrier	Processing
1	Cu–CeO$_2$	68.872	MEK/ethanol+Butvar+Triton	Ball mill (23 h)
2	Cu–LSCM	73.778	Isopropanol+Butvar+Triton	Ball mill (23 h)

1000°C for 5 h with heating and cooling rates at 5°C/min. These were configured as symmetrical cells for AC impedance measurements and were reduced in situ using (dry) 5% H$_2$ in Ar at 700°C before collecting the impedance data, which were also taken under this same reducing atmosphere. Electrode thicknesses were of the order of 80–100 μm as verified by SEM while their geometric area was about 0.97 cm^2. Electrical contact to the electrodes was achieved by means of Pt mesh connected to Pt wire. These experiments were done within a frequency range of 0.1 to 6×10^6 Hz using a Solartron 1287 with 10–20 mV ac signal amplitude. Examples of prepared cermets with calculated pellet porosities and details of processing conditions of slurries are given in Table 2.

Pellets porosities were calculated from pellet geometry and mass, using the theoretical densities of Cu, CuO, LSCM and CeO$_2$.

Thermogravimetric analysis (TGA) was performed on the Cu/LSCM and Cu/CeO$_2$ pellets initially in the oxidized state, under 5% H$_2$/95% Ar at a heating rate of 5°C/min to 900°C. The experiments were performed on a Rheometric TGA2 1000M instrument. Samples were tested by X-ray diffraction for verification of crystal phase by means of a Philips PW 1830 X-ray diffractometer (10°–90° 2θ, Step size 0.5° 2θ, CuK$_{\alpha1}$ radiation). Sample morphology and composition were examined by SEM (JSM-6300 of JEOL) coupled with EDS (ISIS of OXFORD).
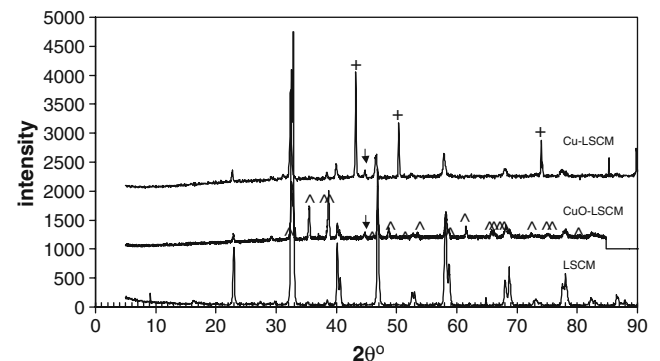
3 Results and discussion

3.1 Phase and reduction behavior of Cu/CeO$_2$ and Cu/LSCM pellets

XRD results for the Cu/CeO$_2$ pellets in the reduced and oxidized state are given in Fig. 1. The bottom line is the pattern exhibited by the oxidized form of the cermet while the top line shows the pattern of the reduced Cu/CeO$_2$ cermet. On the same figure, the peaks corresponding to copper, copper oxide and ceria are also given. In addition, the peaks from the Al sample holder are shown with an arrow. These Al peaks were present in all patterns taken.

It can be seen that for the Cu/CeO$_2$ system the peaks corresponding to the spectra of Cu, CuO and CeO$_2$ resolve clearly and there is no indication of formation of any other phases.

Figure 2 shows the corresponding patterns for the Cu/LSCM cermet. Three lines are shown here, the oxidized (middle) and reduced (top) form of the cermet and the third corresponding to the original LSCM powder pattern. Again, the peaks showing the standard patterns of Cu, CuO and Al are marked on the figure with the same symbols given in Fig. 1. No additional phase formation is observed in this case, as only the major peaks of the constituent phases are clearly resolved. An additional small peak at 31° appeared

Fig. 1 X-ray diffractogram of CuO–CeO$_2$ (*bottom*) and Cu–CeO$_2$ pellets (key ^CuO, *CeO$_2$, +Cu, *arrow* Al sample holder)

Fig. 2 X-ray diffractogram of CuO–LSCM (*middle*) and Cu–LSCM (*top*) pellets and LSCM powder (key ^CuO, +Cu, *arrow* Al sample holder)

after reduction but it does not reflect a significant degree of phase transformation or lattice distortion [30].

The redox behavior of the different cermets was investigated by TGA and the results are shown in Fig. 3. These graphs show change in mass for the oxidized forms of the pellets while they are reduced under hydrogen. It can be seen that the weight loss corresponds exactly to the stoichiometric amount of oxygen in the two cermets (i.e. 9.9% for these compositions) with no measurable weight loss after reduction of CuO. Notice also that for the CuO/LSCM pellet, complete reduction is achieved at 700°C, which is a hundred degrees higher than the corresponding to CuO/CeO$_2$ cermet indicating a slower reduction process for the LSCM cermet. This could reflect a difference in microstructure and subsequent differences in the internal diffusion processes of hydrogen.

3.2 Electrochemical characterization

Slurries of cermets have been prepared and characterized electrochemically on dense YSZ pellets by means of AC impedance.

The AC impedance measurements were taken on a symmetrical YSZ electrode arrangement painted with slurry of either CuO/LSCM or Cu/CeO$_2$ (Slurries # 2 and 1 respectively in Table 1).

Figure 4 shows typical data at temperatures above 570°C for the Cu/CeO$_2$ (top) and the Cu/LSCM cermets. AC spectra obtained at lower temperatures i.e. 280–400°C (not
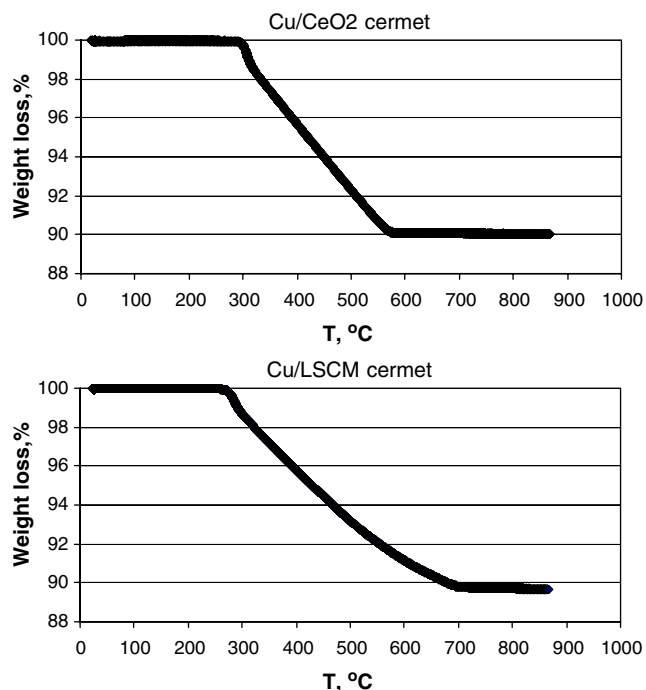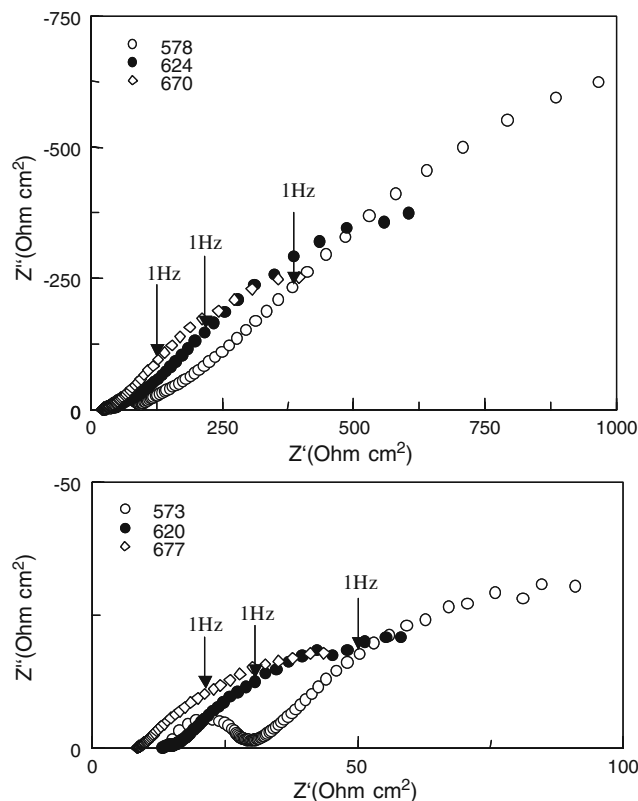
Fig. 4 Typical AC impedance runs for Cu/CeO$_2$ (*top*) and Cu/LSCM symmetrical electrodes on YSZ and under 5% H$_2$ in Ar at temperatures indicated. Frequency range: 0.1 Hz–6 MHz. *Arrows* indicate frequency of 1 Hz

Fig. 3 TGA results for the Cu/CeO$_2$ (*top*) and Cu/LSCM cermets (49% w/w CuO)

shown), generally consist of three arcs, which are typical for an ionic conductor flanked by symmetrical electrodes; the high frequency arc, which is due to the intra-grain electrolyte contribution, the medium frequency arc, which is attributed to the electrolyte grain boundary processes, and the low frequency arc due to electrode processes.

The high frequency arc due to the YSZ electrolyte intra-grain or bulk disappears at about 435–445°C and only the grain boundary arc is observed. Above this temperature, the bulk contribution is just the point of the high frequency intercept of the grain boundary arc with the *x*-axis. This medium frequency arc due to the grain boundary resistance persists up to 620°C. Estimated capacitances for the high frequency arc (i.e. due to the electrolyte bulk contribution), were of the order of $1-4 \times 10^{-12}$ F/cm, while those for the medium frequency (i.e. due to the grain boundary) were of the order of 10^{-9} F/cm. These values were estimated, assuming a circuit consisting of a capacitor in parallel with a resistor, as is typically adopted for solid electrolytes according to Bauerle [60] and using the Instant Fit feature of Z-View software (1990–2002 Scribner Associates Inc.).

The values of the bulk capacitances calculated agree well with those reported for the intra-grain contributions of the YSZ solid electrolyte measured in air. However, grain

boundary capacitances are an order of magnitude lower than those measured in air [61]. This is further discussed below.

The electrode response is not well resolved below 483°C.

Figure 4 shows a difference in the electrode response between the two cermets. Thus, for the Cu/CeO$_2$ cermets the electrode response resembles that of a finite length Warburg type, indicative of a diffusion process. This arc was modeled by a finite length Warburg diffusion element using the Instant Fit of Z-View. This procedure resulted in good fits with errors less than 3% in the estimated polarization resistances.

For the Cu/LSCM cermets, although there is an initial linear part of the electrode arc, this eventually takes the shape of a depressed semicircle as the frequency reaches its minimum value (i.e. 0.1 Hz), something that was not observed in the Cu/CeO$_2$ cermets. Thus, polarization resistances in this case were modeled as circuits (using again the Instant Fit of Z-View) consisting of a CPE in parallel with an ohmic component. This procedure resulted in very good fits (errors <2%) of the electrode arcs. Estimated electrode resistances were lower than those for the Cu/CeO$_2$ cermets while electrode capacitances were of the order of 1×10^{-2} F. The electrode arcs were also modeled by finite length Warburg diffusion elements, in a similar fashion to the Cu/CeO$_2$ electrode arcs. Estimated values by this method were found about 30% smaller than those based on a CPE circuit described previously, but accuracy of the fit was poorer.

Although our main interest is in the polarization resistances of the examined electrodes, a closer examination and comparison of the AC components attributed to the bulk electrolyte could reveal information on electrode–electrolyte contact characteristics since the same electrolyte (YSZ) was used for both electrodes. In view of that, comparison of the characteristic frequencies, capacitances and conductivities for bulk and grain boundary of YSZ, as well as their activation energies, with values from the literature was performed.

The characteristic frequencies (i.e. frequencies at which the imaginary parts of the complex resistances take their maximum values) and capacitances for the bulk and grain boundary components are plotted with respect to reciprocal temperature for both cermets in Fig. 5. It can be seen that characteristic frequencies for both cermets are essentially the same. Both bulk and grain boundary capacitances are generally similar for the Cu–CeO$_2$ and Cu–LCSM cermets at lower temperatures. Errors of estimates from the fits were quite small (i.e. <5%) in all cases and these have been added as error bars on the data of Fig. 5, though their width is of the same magnitude as the symbols used. Goodness of fit was checked by estimating Chi-Squared and Weighted Sum of Squares, which is proportional to the average
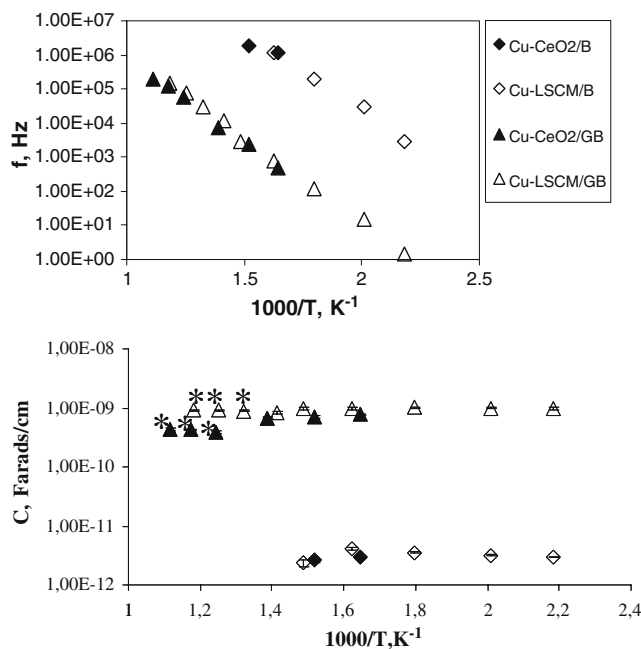

Fig. 5 Characteristic frequencies (*top*) and capacitances taken from the AC impedance data for the Cu–CeO$_2$ and Cu–LSCM symmetrical electrodes with respect to reciprocal absolute temperature (key: *B* bulk, *GB* grain boundary); * denotes significant differences

percentage error between the original data points and the calculated values. It is noteworthy to mention that different fits with varying accuracy gave no more than a ±15% variation in the mean values of the calculated capacitances.

It can be seen that while at low temperatures there are no significant differences between the bulk and grain boundary capacitances estimated from either Cu–LSCM or Cu–CeO$_2$ electrodes, at higher temperature gain boundary capacitances from Cu–CeO$_2$ electrodes seem to be smaller (by almost a factor of 2 to 3) than those estimated on Cu–LSCM electrodes. These differences between capacitance values are statistically significant as has been checked by applying a modified Student *t* test (Welch's approximate *t*) after checking for equality of variances by applying the variance ratio *F*-test [62]. Statistical significance is preserved (at much higher than 95% confidence level) even by using errors of the order of 15% around the mean which is the maximum variation observed by changing the degree of goodness of fit.

The differences observed in the apparent grain boundary capacitances at higher temperatures are probably due to the limited electrode contact in the Cu/CeO$_2$ electrode which is manifested at higher temperatures due to higher oxygen diffusion rates that cannot be accommodated with this particular electrode morphology, resulting in the accumulation of less charge across the interfacial electrode–electrolyte contact area. This is also demonstrated in Fig. 7 below where both the YSZ bulk and grain boundary
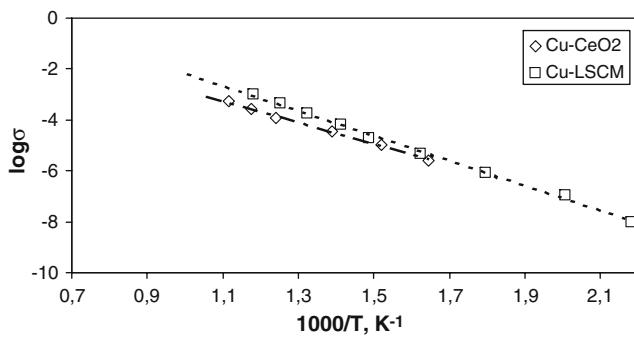
Fig. 6 Arrhenius plots of the YSZ electrolyte total conductivity taken from the AC impedance data for the Cu–CeO₂ and Cu–LSCM electrodes

conductivities measured on Cu–CeO₂ electrodes exhibit lower values than those obtained on the Cu–LSCM anodes at high temperatures.

The ratio of C (bulk)/C (gb) is the same for both electrodes. According to the brick layer model for ceramic microstructures, [63] this ratio is directly proportional to the grain boundary volume fraction within the electrolyte, which, as expected, remains unaffected by the type of electrode. Since these capacitances scale with the ratio of contact area to sample thickness (S/L), it is deduced that actual contact area for the Cu–CeO₂ electrode is less than that of Cu–LSCM electrode. This means that the Cu–CeO₂ cermet exhibits an inferior contact to YSZ than the Cu–LSCM cermet.

Reaction and diffusion between CGO and YSZ has been reported during the sintering process at temperatures of 1200°C [64]. In addition, other authors have found that YSZ and CeO₂ form solid solutions in a wide range of compositions when sintered at 1600°C for 10 h except in the range 40–60% YSZ within which an immiscibility gap exists [65]. On the other hand, He et al. [66] did not detect any new phases in their anode consisted of CeO₂ within an YSZ matrix even after sintering at 1250°C for 2 h. Given that the present cermets are sintered at only 1000°C for 5 h before testing, a reaction between CeO₂ and YSZ does not seem possible in our system.

Figure 6 shows Arrhenius plots of the series resistance, which should correspond, to the YSZ electrolyte total conductivity calculated from data from both cermets. Lines drawn are least square fits. It can be seen that conductivities calculated from the Cu/LSCM symmetrical electrode are generally higher than those taken from the Cu/CeO₂ electrode. This difference is more evident at higher temperatures. Activation energies obtained from this graph were 0.98±0.04 eV for the Cu–LSCM cermet and 0.84±0.08 eV for the Cu–CeO₂ cermet (95% confidence level). The literature activation energy is 1.01±0.03 eV [67] which is the same within error as that calculated above from the Cu–LSCM cermets. On the other hand, the activation energy

taken from the Cu/CeO₂ electrode is different from the literature values and from the value extracted from the Cu–LSCM data.

Figure 7 shows the bulk (top) and grain boundary conductivities for the two cermets.

It can be seen that there is definitely a slight change in slope at around 550°C, which is manifested on the Cu–LSCM electrode, which appears to have a better contact with the electrolyte as mentioned previously. This change in activation energy between low and high temperature is in agreement with the literature and can be explained in terms of the ordering of oxygen vacancy- (dopant) cation clusters that exist at low temperatures to form microdomains [68]. For the Cu/CeO₂ cermets, a larger deviation from the Cu–LSCM values is evident at higher temperatures. Thus, at high temperatures, the bulk conductivity measured on this electrode is lower than that on Cu–LSCM. However, the slopes, and therefore activation energies, seem to be similar to the Cu–LSCM cermet. This could indicate a contact problem in this particular electrode as also identified previously by examining the capacitance behavior (see Fig. 5). This is corroborated by the fact that at lower temperatures, there is an agreement between the conductivity values and activation energies taken from the Cu/CeO₂ and the Cu–LSCM electrode. Thus, the difference observed at higher temperatures is possibly due to the limited electrode contact in the Cu/CeO₂ electrode, which is manifested at higher temperatures due to higher oxygen
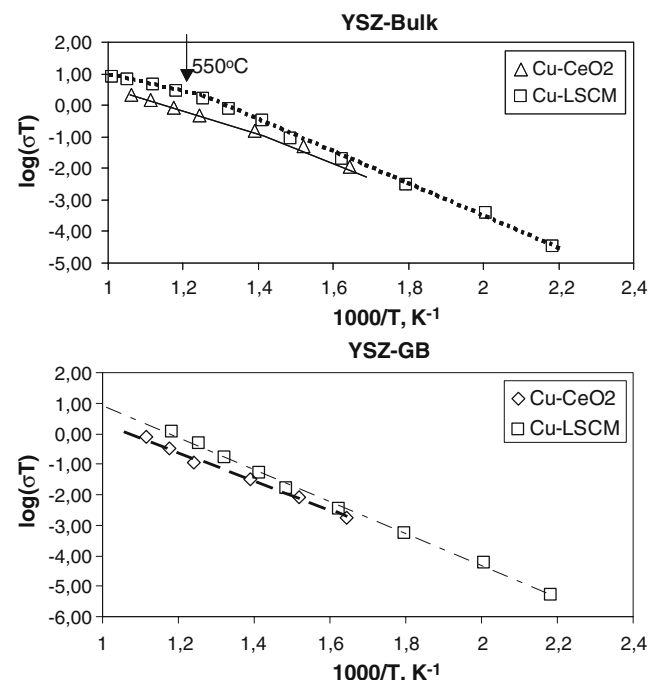

Fig. 7 Arrhenius plots of the YSZ electrolyte bulk (*top*) and grain boundary conductivities taken from the AC impedance data

diffusion rates that cannot be accommodated with this particular electrode morphology. Activation energies measured for the Cu–LSCM electrodes were 0.99 ± 0.05 eV for $T < 550°C$ and 0.58 ± 0.10 eV for $T > 550°C$. The corresponding values for the Cu/CeO$_2$ cermet were 1.0 ± 0.2 and 0.74 ± 0.05 eV. These have to be compared with 1.06 and 0.92 eV for the low and high temperature range respectively in reference [68]. Notice the lower activation energy measured in our data for the high temperature range, which could also be attributed to a worse electrode contact revealing its effect at these temperatures.

Grain boundary conductivities measured in this study (Fig. 7, bottom) are quite low and in fact, grain boundary resistances account for about 64–86% of the total series resistance. This is due to the fabrication method, impurities and type of the precursors used for the staring powders of this electrolyte. Activation energies for the grain boundary conductivities estimated from our data were 1.04 ± 0.05 for the Cu–LSCM cermet and 0.95 ± 0.10 eV for the Cu/CeO$_2$ cermet. Notice also that at higher temperatures the deviation between grain boundary conductivities extracted from Cu–CeO$_2$ and Cu–LSCM increases, most possibly due to again the inferior contact of the Cu–CeO$_2$ electrode to the YSZ electrolyte. This has also been observed at the top part of the same figure for the bulk conductivities.

It is concluded that the difference found for the total conductivity values is due to the differences in the bulk and grain boundary conductivities becoming more significant above 550°C where the inferior contact of the Cu–CeO$_2$ electrode with the YSZ electrolyte is manifested more clearly.

Figure 8 shows polarization resistances for the two cermets measured on YSZ electrolyte. In the examined low temperature range (i.e. 480–720°C) the best values were found for the Cu–LSCM electrode and were within of 27–200 Ω cm^2. These values are, actually, quite similar to conventional Ni–YSZ anodes (in wet H$_2$ and measured by AC Impedance under open circuit) which should exhibit
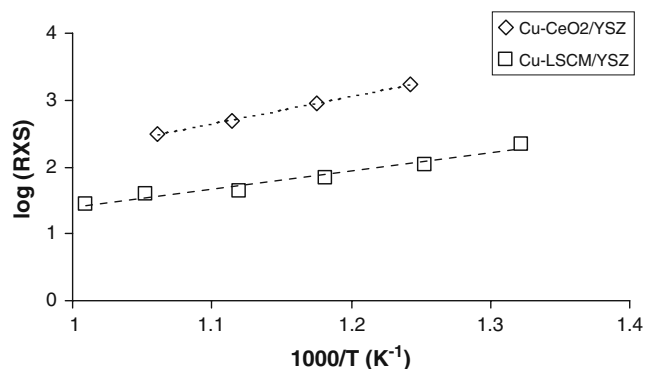
polarization resistances of the order of 1–30 Ω cm^2 at 700°C and 7–200 Ω cm^2 at 600°C as extrapolated from the data collected in the review by Jiang and Chan [37].

These relatively high resistances are due to the lower temperature range investigated in these experiments.

Poor performance was observed for the Cu/CeO$_2$ electrode, which exhibited polarization resistances, almost an order of magnitude higher than those corresponding to the Cu–LSCM electrode. A possible contact problem between the Cu/CeO$_2$ electrode and the YSZ electrolyte as suggested previously could contribute in these high polarization resistances measured on this electrode. Electrode morphology also plays a role and this is further discussed below.

It has to be emphasized, here, that both Cu–CeO$_2$ and Cu–LSCM films showed good adhesion with the electrolyte since they were reduced at 700°C. So as long as the reduction temperature remains ≤700°C no delamination is observed for both electrodes despite their relatively high Cu content (i.e. about 70% w/w CuO). This is also discussed in the Section 3.4.1 (Film morphology). In fact, after this initial reduction at low temperature and the end of the AC Impedance experiments, the Cu–CeO$_2$ film remained adherent to the electrolyte after being re-oxidized and re-reduced at even at 900°C for ½ h, with Cu interconnectivity being still quite good though with some degree of Cu segregation evident possibly due to the higher re-reduction temperatures employed. Thus, the inferior contact between Cu–CeO$_2$ and YSZ electrolyte does not result in delamination as long as the reduction temperature is ≤700°C. Reduction temperatures for Cu–CeO$_2$ cermets can be as low as 600°C as shown in the TGA results of Fig. 3 which means that good adherence can be achieved by reduction at lower temperatures and simultaneous preservation of suitable electrode microstructure.
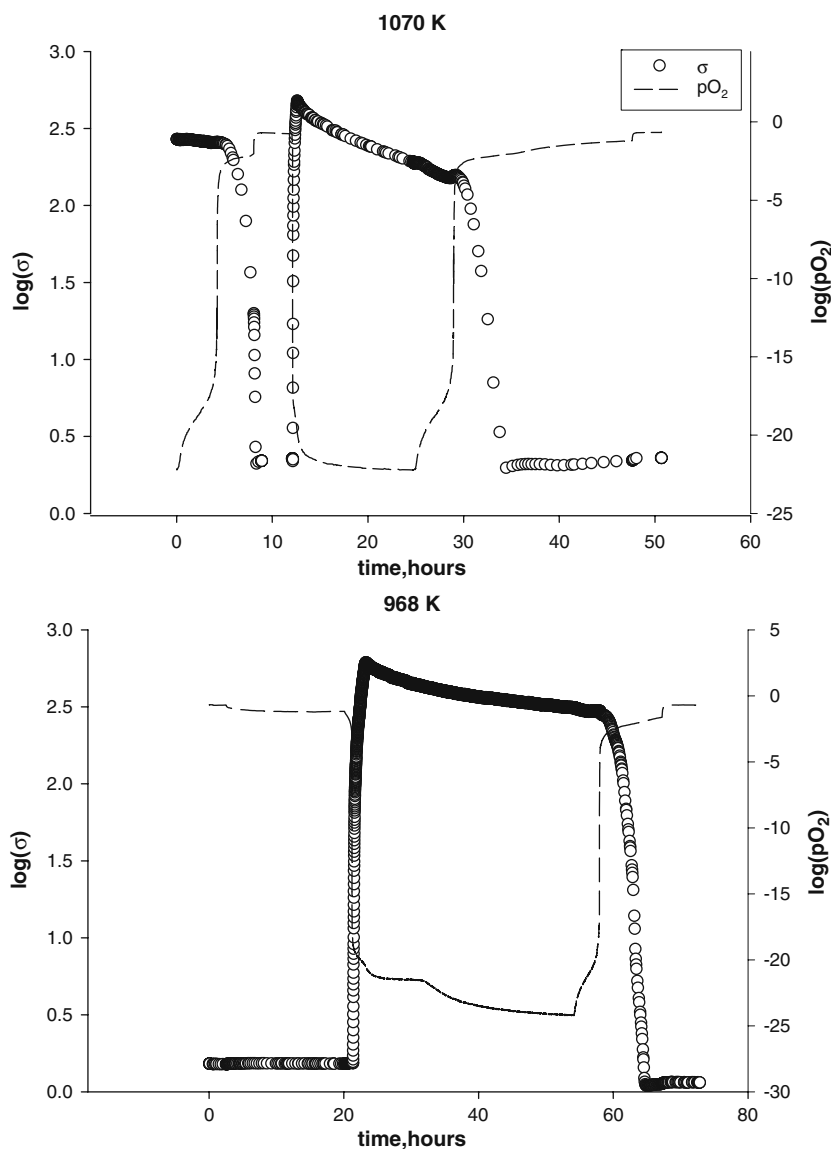
This inferior contact between the Cu–CeO$_2$ and the YSZ electrolyte, may in fact, be due to a non-optimized microstructure, which is due to the different starting powder properties in this particular electrode, and eventually, result in inferior polarization performance with respect to the Cu–LSCM electrode. This is corroborated by the fact, that Cu–CeO$_2$ anodes developed by Gorte and collaborators fabricated differently and thus, exhibiting a different microstructure, [39–43] showed superior values of anodic polarization resistances under CH$_4$, C$_4$H$_{10}$, CO or synthesis gas in the temperature range 700–800°C. Also, anodic polarization resistance values under H$_2$ for Cu–CeO$_2$ electrodes are reported between 0.1 and 0.8 Ω cm^2 (see Table 1) and compare favorably with those of Ni–YSZ. However, it has also been found by these authors, that annealing under H$_2$ at temperatures above 700°C results in significant drops in fuel cell performance of Cu/CeO$_2$/YSZ cermets prepared as described above. At 900°C Cu

Fig. 8 Arrhenius plots of the specific (Ohm cm^2) AC polarization resistances for the Cu–CeO$_2$ and Cu–LSCM electrodes on YSZ

segregation is severe, forming either isolated particles or even extended porous films near the YSZ surface [17–19]. Therefore, we believe that the reason for the poorer performance of Cu–CeO$_2$ electrodes in our case is most probably due to the inferior microstructure of the cermet.

Activation energies obtained from the slopes of the lines of Fig. 8 were found to be 0.5±0.2 eV for the Cu/LSCM electrode and 0.8±0.1 eV for the Cu–CeO$_2$ electrode (confidence level 95%). These differences suggest a different charge transfer reaction mechanism occurring on the two electrodes. However, more work is definitely required in order to further clarify this point and in particular electrochemical testing under current load conditions.

It is concluded that, electrochemical performance as viewed in terms of polarization resistance of slurries consisting of Cu–LSCM cermets is superior compared to Cu/CeO$_2$ cermets.

3.3 Conductivity measurements of thick Cu–LSCM pellets

In order to further investigate the performance of the Cu–LSCM cermet as an anodic support, we examined its conductivity behavior of a pellet (pellet #3 in Table 1) under redox cycling by means of four-point DC measurements.

Previous work [21] regarding percolation limits on Cu–Y$_{0.2}$Ti$_{0.18}$Zr$_{0.62}$O$_{1.9}$ (Cu–YZT) showed that pellets become conductive above about 50% w/w CuO which corresponds to about 33.6% v/v Cu after reduction. This is above the percolation threshold as it was established for Ni cermets [69]. Similarly, pellets of Cu/CeO$_2$ and Cu–LSCM were conductive above about 49% CuO w/w, which corresponded to about 39.6% and 34.4% v/v Cu after reduction. These calculations were based on the theoretical densities Cu, CuO, CeO$_2$ and LSCM being taken as: Cu: 8.94, CuO: 6.31, CeO$_2$: 7.65 and LSCM: 6.51 g/cm^3.

Fig. 9 Four-point DC conductivity of a Cu–LSCM (49.2% w/w CuO) pellet under redox cycling along with P$_{O2}$ values obtained, at two temperatures
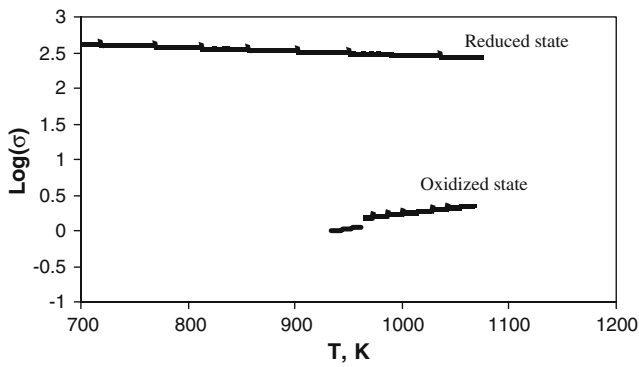
Fig. 10 Effect of temperature on a Cu–LSCM (49.2% w/w CuO) pellet conductivity under reduced and oxidized conditions from four-point DC conductivity data

increase in conductivity above the final value during reduction may well be due to some cooling process during the reduction as the 5% H_2 is introduced.

Measurements were taken during three complete redox cycles and included 72 h anneal at 968 K under reducing conditions. The pellet remained for a total of 7 days under redox cycling with no apparent mechanical degradation and no significant change in conductivity in either reduced or oxidized conditions.

Figure 10 shows the effect of temperature on cermet conductivity under reduced (top trace) and oxidizing conditions. The conductivity of the reduced pellet remains high (at about 300 S/cm) and decreases slightly with increasing temperature as expected for a metal (Cu) dominated cermet with a calculated coefficient of 0.0046/°C.

Generally, the above results show that these bulk cermets exhibit good thermal and redox cycling behavior in terms of retention of electrical conductivity. Mechanical integrity and handling strength was also preserved after redox cycling and TGA. No significant overall shrinkage and expansion was measured (geometrically) in either Cu–LSCM or Cu–CeO$_2$ pellets after reduction (i.e. <±2% v/v). More work is required in order to assess their mechanical integrity under redox cycling and particularly dilatometric measurements as a function of PO_2 to effectively assess shrinkage and expansion behavior.
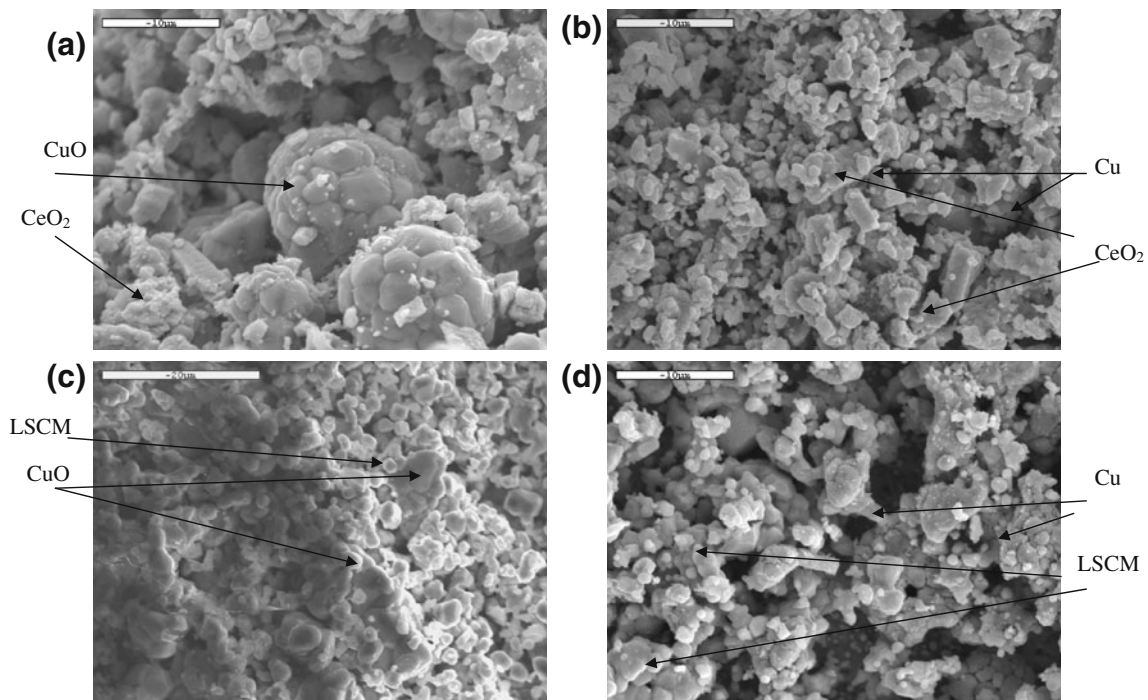
Figure 9 shows redox cycling behavior for the Cu–LSCM composite at 1070 K and 968 K. At 1070 K, an initially reduced pellet was oxidized with conductivity decreasing by two to three orders of magnitude on oxidation of Cu. Similar behavior is observed at 968 K. In this case, the process had started from the oxidized state ($pO_2 = 0.21$ atm). Notice that in both figures there is always a difference in the pO_2 value at which conductivity changes (i.e. inflection points on the pO_2 curves), depending on the initial state (i.e. oxidized or reduced). This is hysteresis due to kinetic limitations at both temperatures. The slight

Fig. 11 SEM images of the film cermets; (a) CuO–CeO$_2$, (b) Cu–CeO$_2$, (c) CuO–LSCM, (d) Cu–LSCM (*scale bars*: **a**, **b**, **d**=10 μm, **c**=20 μm)

3.4 Electrode morphology

3.4.1 Film morphology

Electrode thicknesses of samples used for AC impedance measurements were measured by SEM to be in the range of 80–100 μm. These relatively large electrode thicknesses could produce a slow diffusion process, which was indeed observed at the high frequency part of the electrode response in the AC impedance runs.

Figure 11 shows SEM images of the cermets in their oxidized (left) and reduced forms. The Cu–CeO$_2$ cermet is shown on the top. The larger agglomerates shown in the oxidized forms of the cermets correspond to CuO particles in both cases. Ceramic particles appear to be more uniform in size (1–2 μm). Good adhesion between the electrode and electrolyte was generally, observed for both cermets in their oxidized state.

Surface images after reduction are shown on the right. Reduction was achieved at 750°C for 1 h under 5% H$_2$ in Ar for both cermets. It can be seen that porosities significantly increase after reduction. Higher porosities are observed for the Cu–LSCM electrode. In addition, Cu distribution seems to be somehow better for the Cu–LSCM surface compared to the Cu–CeO$_2$ surface, which seems to contain less Cu. This was verified by comparison of the EDS mappings (not shown) of several spots on the film surfaces. It was also observed after reduction, that better adhesion to the YSZ electrolyte surface is exhibited by the Cu–LSCM electrode than the Cu–CeO$_2$ electrode, which easily flaked off at several spots on the surface. This could indicate somehow a higher degree of Cu mobility or segregation occurring on the Cu–CeO$_2$ electrode.

Cross sections of the electrodes are shown in Fig. 12. In addition, Fig. 13 shows EDS mappings of the interface for the metal and ceramic parts. These films were used for the AC Impedance measurements. The Cu–LSCM electrode is shown at the bottom of the figures. This film was reduced at 700°C. Cu distribution and interconnectivity seem quite satisfactory throughout the film body. This also explains the superior performance of this electrode in terms of AC measured polarization resistance.

The Cu–CeO$_2$ film was also reduced originally at 700°C but then oxidized and subsequently re-reduced according to the following profile: ½ h at 900, ½ 800, ½ h 700 and ½ 600°C before cooled down. It can be seen that Cu distribution is different here with Cu interconnectivity being still quite good though with some degree of Cu segregation evident possibly due to the higher re-reduction temperatures employed.

To further explore this temperature effect, films of both cermets were fabricated and reduced at 900°C. This procedure resulted in bad quality films with almost no adhesion onto YSZ and nearly complete separation of Cu and the ceramic.

In conclusion, these cermet electrode films have to be reduced at temperatures ≤750°C in order to assure good adhesion and suitable microstructure. At temperatures higher than 750°C Cu might become mobile and segregate, resulting in a poor microstructure and/or peeling off. Reduction temperature seems to affect to a greater extent Cu–CeO$_2$ films, which exhibited some degree of Cu segregation even at 750°C. This could be due to the expansion [70] of CeO$_2$ lattice during reduction and its larger thermal expansion coefficient mismatch to the YSZ electrolyte resulting in the peeling off of the electrode.

3.4.2 Pellet morphology

Pellets were also examined by SEM/EDS and Fig. 14 shows typical microstructures obtained for Cu–CeO$_2$ (top) and Cu–LSCM pellets. The oxidized forms of the pellets are shown on the left. These were sintered at 1000°C for 10 h. This procedure results in pellets with relatively low porosities (i.e. ~33% for CuO–LSCM and ~21% for CuO–CeO$_2$ as shown in Table 2). Larger agglomerates correspond to CuO particles as indicated on the figures.
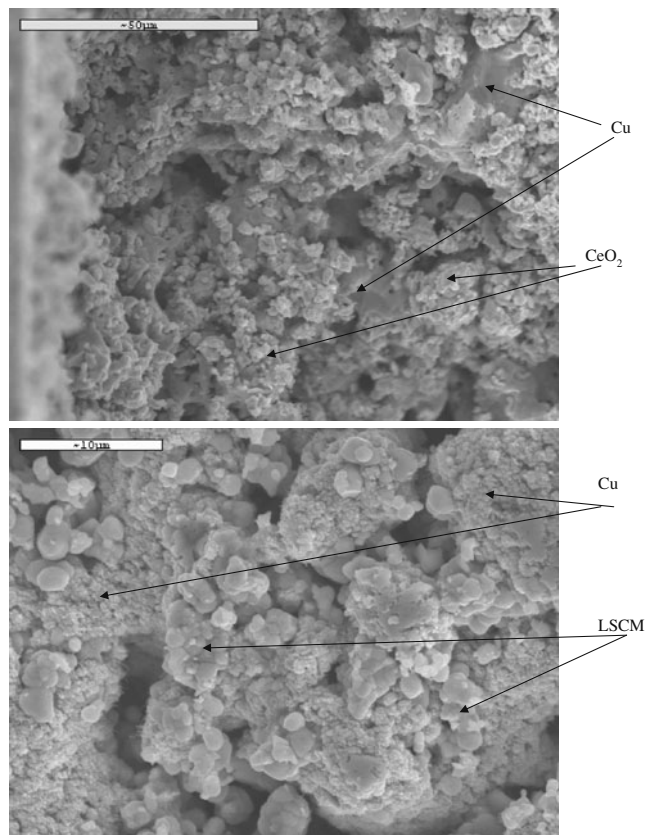

Fig. 12 SEM images of cross-sections of the Cu–CeO$_2$ (*top*) and Cu–LSCM film electrodes in their reduced state
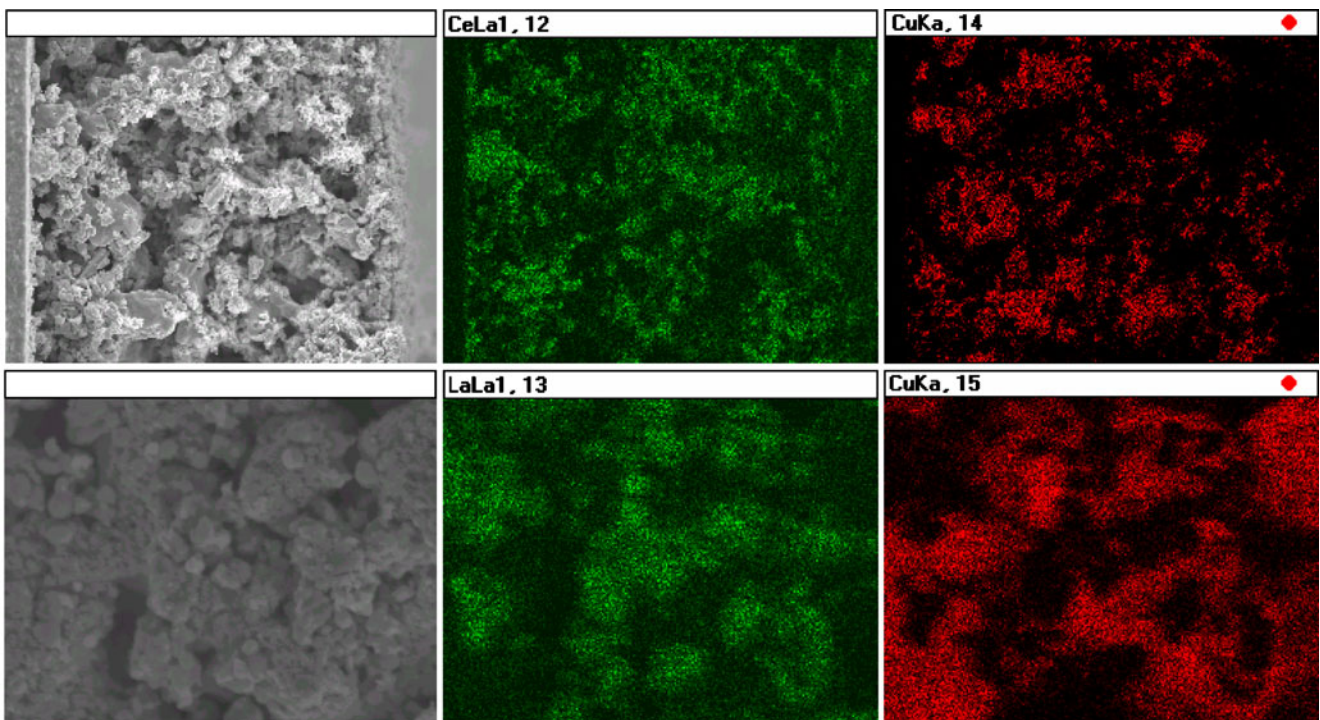
Fig. 13 EDS mappings of cross sections of Cu–CeO$_2$ (*top*) and Cu–LSCM film cermets

On the right, the corresponding microstructures after reduction at 800°C for 1 h in 5% H$_2$ in Ar are shown. Here porosities are higher and reach about 50% for Cu–LSCM and 43% for Cu–CeO$_2$ (see Table 2). It can be seen that Cu aggregates constitute a network with good interconnectivity resulting in high conductivity for both cermets. This was verified by EDS mapping of the examined surfaces (not shown). Both types of pellets retain their mechanical strength and fracture resistance after reduction.
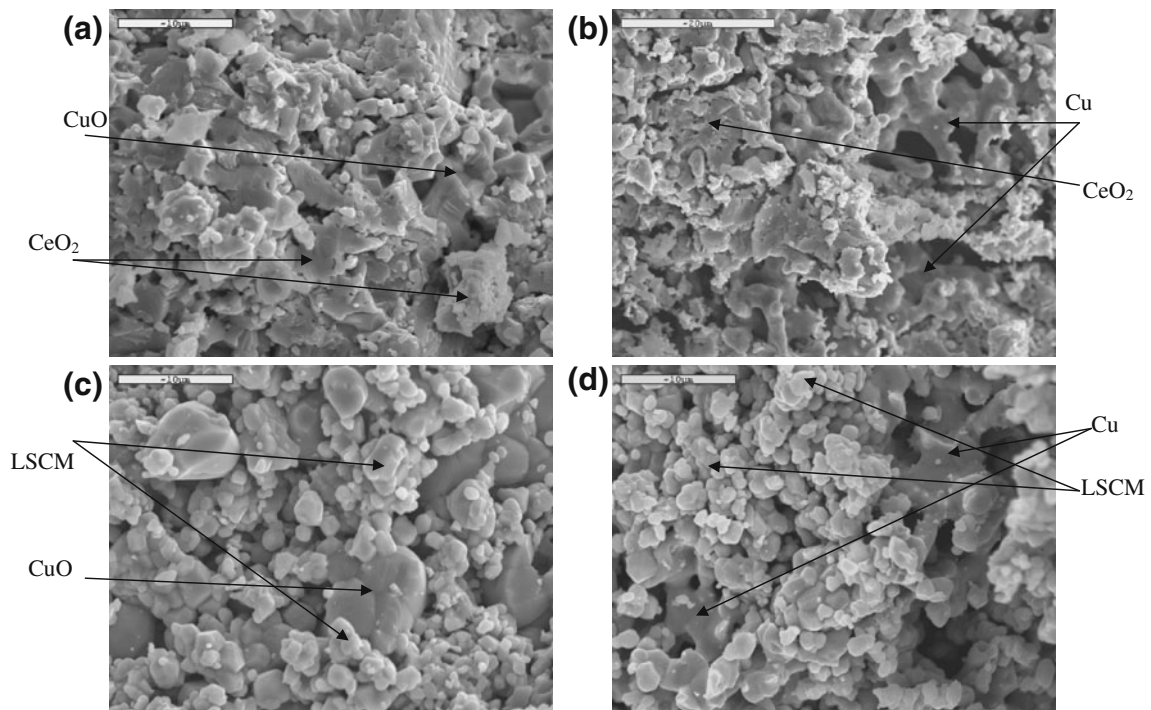
Fig. 14 SEM images of the pellet cermets; (**a**) CuO–CeO$_2$, (**b**) Cu–CeO$_2$, (**c**) CuO–LSCM, (**d**) Cu–LSCM (*scale bars*: **a**, **c**, **d**=10 μm, **b**=20 μm)

4 Conclusions

Results are presented on the behavior of two different Cu based cermets as anodes in YSZ based Solid Oxide Fuel Cells at an intermediate temperature range (i.e. 500–800°C). These electrodes would be suitable for direct hydrocarbon oxidation in Solid Oxide Fuel Cells since they combine the inertness of Cu in avoiding cracking reactions and the mixed conductivity and favorable catalytic properties of their ceramic counterparts, which were the perovskite $La_{0.75}Sr_{0.25}Cr_{0.5}Mn_{0.5}O_{3-d}$ and CeO_2.

It was found that under H_2, Cu–LSCM shows a superior behavior to that of Cu–CeO_2 in terms of polarization resistance measured by AC impedance. This is corroborated by the superior morphology of the former electrode as examined by SEM and EDS, which showed a good dispersion, and interconnectivity of Cu particles with the cermet structure. In contrast, Cu segregation was more obvious in the Cu–CeO_2 cermets with Cu tending to form isolated regions within the cermet structure.

Reduction temperature has a significant effect on final film morphology. It was found that these cermets have to be reduced at temperatures ≤750°C for good adhesion with the YSZ electrolyte and to form a suitable microstructure.

Cu–LSCM cermets were also tested in the form of pellets and their redox behavior was examined by means of four-point DC conductivity. It was found that this cermet could work as a suitable anodic support achieving a conductivity of about 300 S/cm in the reduced state, and withstanding quite well redox cycling with no apparent mechanical degradation. Finally, there was no indication of formation of other phases by XRD in both cermets even after treatment at 1000°C for 10 h in air. Porosity of the pellets favored again the Cu–LSCM cermets, while both showed adequate mechanical strength and resistance to fracture after reduction. Cu segregation is visible at reduction temperatures ≥800°C for both cermets.

Future work will be focused in examining the behavior of these anodes under fuel cell operating conditions in a two or three electrode arrangement. This will include testing under various current loads and evaluation of their performance under methane and other types of hydrocarbon. In addition, since polarization resistances are still quite high for this temperature range, further research is needed for a more optimized microstructure and/or more efficient electrocatalysts. One approach towards this goal is substituting LSCM with a composite of LSCM with YSZ and $Ce_{0.8}Gd_{0.2}O_{2-\delta}$ (CGO20) (CGO) [27]. This type of work is currently under progress.

References

1. B.C.H. Steele, A. Heinzel, Nature. **414**, 345 (2001). doi:10.1038/35104620
2. M. Stoukides, Catal. Rev. Sci. Eng. **42**(1&2), 1 (2000). doi:10.1081/CR-100100259
3. A.L. Sauvet, J.T.S. Irvine, Solid. State. Ion. **167**, 1 (2004). doi:10.1016/j.ssi.2003.11.021
4. A. Atkinson, S. Barnett, R.J. Gorte, J.T.S. Irvine, A.J. McEvoy, M. Mogensen, S.C. Singhal, J. Vohs, Nat. Mater. **3**, 17 (2004). doi:10.1038/nmat1040
5. S. McIntosh, R.J. Gorte, Chem. Rev. **104**, 4845 (2004). doi:10.1021/cr020725g
6. M. Mogensen, S. Primdahl, M.J. Jørgensen, C. Bagger, J. Electroceram. **5**(2), 141 (2000). doi:10.1023/A:1009910202330
7. S. Hamakawa, T. Hayakawa, A.P.E. York, T. Tsunoda, Y.S. Yoon, K. Suzuki, M. Shimizu, K. Takehira, J. Electrochem. Soc. **143**(4), 1264 (1996). doi:10.1149/1.1836627
8. M. Stoukides, Ind. Eng. Chem. Res. **27**(10), 1745 (1988). doi:10.1021/ie00082a002
9. E. Ramirez-Cabrera, A. Atkinson, D. Chadwick, Solid. State. Ion. **136**, 825 (2000). doi:10.1016/S0167-2738(00)00507-5
10. O.A. Marina, M. Mogensen, Appl. Catal. A. **189**, 117 (1999). doi:10.1016/S0926-860X(99)00259-8
11. S.D. Park, J.M. Vohs, R.J. Gorte, Nature. **404**, 265 (2000). doi:10.1038/35005040
12. H. Kim, S. Park, J.M. Vohs, R.J. Gorte, J. Electrochem. Soc. **148**, A693 (2001). doi:10.1149/1.1374216
13. S. Park, R.J. Gorte, J.M. Vohs, Appl. Catal. A **200**, 55 (2000). doi:10.1016/S0926-860X(00)00650-5
14. R.J. Gorte, S. Park, J.M. Vohs, C. Wang, Adv. Mater. **12**, 1465 (2000). doi:10.1002/1521-4095(200010)12:19<1465::AID-ADMA1465>3.0.CO;2-9
15. S. McIntosh, J.M. Vohs, R.J. Gorte, Electrochim. Acta. **47**, 3815 (2002). doi:10.1016/S0013-4686(02)00352-3
16. H. He, R.J. Gorte, J.M. Vohs, Electrochem. Solid-State. Lett. **8**(6), A279 (2005). doi:10.1149/1.1896469
17. M.D. Gross, J.M. Vohs, R.J. Gorte, J. Electrochem. Soc. **153**, A1386 (2006). doi:10.1149/1.2201534
18. S. Jung, C. Lu, H. He, K. Ahn, R.J. Gorte, J.M. Vohs, J. Power Sources **154**, 42 (2006). doi:10.1016/j.jpowsour.2005.04.018
19. M.D. Gross, J.M. Vohs, R.J. Gorte, Electrochim. Acta **52**, 1951 (2007). doi:10.1016/j.electacta.2006.08.005
20. O. Costa-Nunes, R.J. Gorte, J.M. Vohs, J. Mater, Chem. **15**, 1520 (2005). doi:10.1039/b416670a
21. N. Kiratzis, P. Holtappels, C.E. Hatchwell, M. Mogensen, J.T.S. Irvine, Fuel. Cells. (Weinh.). **1**, 211 (2001). doi:10.1002/1615-6854(200112)1:3/4<211::AID-FUCE211>3.0.CO;2-H

22. J.T.S. Irvine, A. Sauvet, Fuel. Cells. (Weinh.). **1**, 205 (2001). doi:10.1002/1615-6854(200112)1:3/4<205::AID-FUCE205>3.0. CO;2-5

23. N.Q. Minh, J. Am. Ceram. Soc. **76**(3), 563 (1993). doi:10.1111/j.1151-2916.1993.tb03645.x

24. H. Yokokawa, N. Sakai, T. Kawada, M. Dokiya, Solid. State. Ion. **52**, 43 (1992). doi:10.1016/0167-2738(92)90090-C

25. J. Sfeir, P.A. Buffat, P. Mockli, N. Xanthopoulos, R. Vasquez, H.J. Mathieu, J. Van herle, K.R. Thampi, J. Catal. **202**, 229 (2001). doi:10.1006/jcat.2001.3286

26. S. Tao, J.T.S. Irvine, Nat. Mater. **2**, 320 (2003). doi:10.1038/nmat871

27. S. Tao, J.T.S. Irvine, J. Electrochem. Soc. **151**(2), A252 (2004). doi:10.1149/1.1639161

28. V.V. Kharton, E.V. Tsipis, I.P. Marozau, A.P. Viskup, J.R. Frade, J.T.S. Irvine, Solid State Ion. **178**, 101 (2007). doi:10.1016/j.ssi.2006.11.012

29. E.S. Raj, J.A. Kilner, J.T.S. Irvine, Solid State Ion. **177**, 1747 (2006). doi:10.1016/j.ssi.2006.04.011

30. S. Tao, J.T.S. Irvine, Chem. Mater. **18**, 5453 (2006). doi:10.1021/cm061413n

31. S.M. Plint, P.A. Connor, S. Tao, J.T.S. Irvine, Solid State Ion. **177**, 2005 (2006). doi:10.1016/j.ssi.2006.02.025

32. S. Tao, J.T.S. Irvine, S.M. Plint, J. Phys. Chem. B **110**, 21771 (2006). doi:10.1021/jp062376q

33. D.M. Bastidas, S. Tao, J.T.S. Irvine, J. Mater. Chem. **16**, 1603 (2006). doi:10.1039/b600532b

34. J.C. Ruiz-Morales, J. Canales-Vázquez, B. Ballesteros-Pérez, J. Peña-Martínez, D. Marrero-López, J.T.S. Irvine, P. Núñez, J. Eur. Ceram. Soc. **27**, 4223 (2007). doi:10.1016/j.jeurceramsoc.2007.02.117

35. J.C. Ruiz-Morales, J. Canales-Vázquez, D. Marrero-López, J.T.S. Irvine, P. Núñez, Electrochim. Acta. **52**, 7217 (2007). doi:10.1016/j.electacta.2007.05.060

36. S. Primdahl, M. Mogensen, Solid. State. Ion **152–153**, 597 (2002). doi:10.1016/S0167-2738(02)00393-4

37. S.P. Jiang, S.H. Chan, J. Mater. Sci. **39**, 4405 (2004). doi:10.1023/B:JMSC.0000034135.52164.6b

38. E.P. Murray, T. Tsai, S.A. Barnett, Nature. **400**, 649–651 (1999). doi:10.1038/21781

39. S. McIntosh, J.M. Vohs, R.J. Gorte, J. Electrochem. Soc. **150**(10), A1305 (2003). doi:10.1149/1.1603246

40. R.J. Gorte, J.M. Vohs, S. McIntosh, Solid. State. Ion. **175**, 1 (2004). doi:10.1016/j.ssi.2004.09.036

41. S.-I. Lee, J.M. Vohs, R.J. Gorte, J. Electrochem. Soc. **151**(9), A1319 (2004). doi:10.1149/1.1774184

42. S.-I. Lee, K. Ahn, J.M. Vohs, R.J. Gorte, Electrochem. Solid-State Lett. **8**, A48 (2005). doi:10.1149/1.1833678

43. O. Costa-Nunes, R.J. Gorte, J.M. Vohs, J. Power Sources **141**, 241 (2005). doi:10.1016/j.jpowsour.2004.09.022

44. C. Sun, U. Stimming, J. Power Sources **171**, 247 (2007). doi:10.1016/j.jpowsour.2007.06.086

45. S.P. Jiang, X.J. Chen, S.H. Chan, J.T. Kwok, J. Electrochem. Soc. **153**, A850 (2006). doi:10.1149/1.2179347

46. H.J. Cho, G.M. Choi, J. Power. Sources. **176**, 96 (2008). doi:10.1016/j.jpowsour.2007.09.118

47. B.C.H. Steele, J. Mater. Sci. **36**, 1053 (2001). doi:10.1023/A:1004853019349

48. Y. Jiang, A.V. Virkar, J. Electrochem. Soc. **150**(7), A942 (2003). doi:10.1149/1.1579480

49. T. Tsai, S.A. Barnett, Solid State Ion. **98**, 191 (1997). doi:10.1016/S0167-2738(97)00113-6

50. J. Liu, S.A. Barnett. Solid State Ion. **158**, 11 (2003). doi:10.1016/S0167-2738(02)00769-5

51. H. Kim, C. Lu, W.L. Worrell, J.M. Vohs, R.J. Gorte. J. Electrochem. Soc. **149**(3), A247 (2002). doi:10.1149/1.1445170

52. E.P. Murray, S.J. Harris, J. Liu, S.A. Barnett. Electrochem. Solid-State Lett. **9**(6), A292 (2006). doi:10.1149/1.2192643

53. J.C. Ruiz-Morales, J. Canales-Vázquez, J. Peña-Martínez, D. Marrero-López, P. Núñez. Electrochim. Acta **52**(1), 278 (2006). doi:10.1016/j.electacta.2006.05.006

54. H. Tu, U. Stimming. J. Power Sources **127**, 284 (2004). doi:10.1016/j.jpowsour.2003.09.025

55. T. Kawada, N. Sakai, H. Yokokawa, M. Dokiya, M. Mori, T. Iwata. J. Electrochem. Soc. **137**(10), 3042 (1990). doi:10.1149/1.2086156

56. V. Krishnan, S. McIntosh, R.J. Gorte, J.M. Vohs. Solid State Ion. **166**(1–2), 191 (2004). doi:10.1016/j.ssi.2003.10.007

57. A. Weber, B. Sauer, A.C. Müller, D. Herbstritt, E. Ivers-Tiffée, Solid. State. Ion **152–153**, 543 (2002). doi:10.1016/S0167-2738(02)00359-4

58. S. Park, R. Cracium, J.M. Vohs, R.J. Gorte. J. Electrochem. Soc. **146**(10), 3603 (1999). doi:10.1149/1.1392521

59. Y. Matsuzaki, I. Yasuda. Solid State Ion. **132**, 261 (2000). doi:10.1016/S0167-2738(00)00653-6

60. J.E. Bauerle, J. Phys. Chem. Solids. **30**, 2657 (1969). doi:10.1016/0022-3697(69)90039-0

61. I. Gibson, PhD Thesis, U. Aberdeen (1995)

62. J.H. Zar, *Biostatistical Analysis*, 4th edn. (Prentice-Hall, New Jersey, 1999)

63. J.R. Macdonald, *Impedance Spectroscopy: Theory, Experiments and Applications* (Wiley, New Jersey, 1987)

64. A. Tsoga, A. Naoumidis, D. Stover. Solid State Ion. **135**, 403 (2000). doi:10.1016/S0167-2738(00)00477-X

65. N.M. Sammes, G.A. Tompsett, Zhihong Cai. Solid State Ion. **121**, 121 (1999). doi:10.1016/S0167-2738(98)00538-4

66. H. He, J.M. Vohs, R.J. Gorte. J. Electrochem. Soc. **150**, A1470 (2003). doi:10.1149/1.1614268

67. O.H. Kwon, G.M. Choi. Solid State Ion. **177**, 3057 (2006). doi:10.1016/j.ssi.2006.07.039

68. I.R. Gibson, J.T.S. Irvine. J. Mater. Chem. **6**, 895 (1996). doi:10.1039/jm9960600895

69. D.W. Dees, T.D. Claar, T.E. Easler, D.C. Fee, F.C. Mrazek. J. Electrochem. Soc. **134**(9), 2141 (1987). doi:10.1149/1.2100839

70. M. Mogensen, T. Lindegaard, U.R. Hansen, G. Mogensen. J. Electrochem. Soc. **141**(8), 2122 (1994). doi:10.1149/1.2055072